Critical Interactions Between the SARS-CoV-2 Spike Glycoprotein and the Human ACE2 Receptor

Authors

E. Taka[1]†, S. Z. Yilmaz[1]†, M. Golcuk[1]†, C. Kilinc[1], U. Aktas[1], A. Yildiz[2,3], M. Gur[1]*

Affiliations

[1] Department of Mechanical Engineering, Istanbul Technical University (ITU), Istanbul, Turkey

[2] Physics Department, University of California, Berkeley, CA, USA

[3] Department of Molecular and Cellular Biology, University of California, Berkeley, CA, USA

* Corresponding author. Email: gurme@itu.edu.tr

† These authors contributed equally to this work

Abstract

Severe acute respiratory syndrome coronavirus 2 (SARS-CoV-2) enters human cells upon binding of its spike (S) glycoproteins to ACE2 receptors and causes the coronavirus disease 2019 (COVID-19). Therapeutic approaches to prevent SARS-CoV-2 infection are mostly focused on blocking S-ACE2 binding, but critical residues that stabilize this interaction are not well understood. By performing all-atom molecular dynamics (MD) simulations, we identified an extended network of salt bridges, hydrophobic and electrostatic interactions, and hydrogen bonding between the receptor-binding domain (RBD) of the S protein and ACE2. Mutagenesis of these residues on the RBD was not sufficient to destabilize binding but reduced the average work to unbind the S protein from ACE2. In particular, the hydrophobic end of RBD serves as the main anchor site and unbinds last from ACE2 under force. We propose that blocking this site via neutralizing antibody or nanobody could prove an effective strategy to inhibit S-ACE2 interactions.

Introduction

The COVID-19 pandemic is caused by SARS-CoV-2, which is a positive-sense single-stranded RNA betacoronavirus. Phylogenetic analyses demonstrated that the SARS-CoV-2 genome shares ~79% sequence identity with severe acute respiratory syndrome coronavirus (SARS-CoV), and ~52% with the Middle-East respiratory syndrome coronavirus (MERS-CoV)[1]. Despite these similarities, SARS-CoV-2 is much more infectious and fatal than SARS-CoV and MERS-CoV together[2].

SARS-CoV-2 consists of a 30 kb single-stranded RNA genome that is encapsulated by a lipid bilayer and three distinct structural proteins that are embedded within the lipid membrane: envelope (E), membrane (M), and spike (S). Host cell entry is primarily mediated by homotrimeric S glycoproteins located on the viral membrane (Fig. 1a)[3]. Each S protomer consists of S1 and S2 subunits that mediate binding to the host cell receptor and fusion of the viral envelope, respectively[3, 4]. The receptor-binding domain (RBD) of S1 undergoes a large rigid body motion to bind to ACE2. In the closed state, all RBDs of the S trimer are in the down position, and the binding surface is inaccessible to ACE2. The switching of one of the RBDs into a semi-open intermediate state is sufficient to expose the ACE2 binding surface and stabilize the RBD in its up position (Fig. 1b)[5].

The S protein binds to the human angiotensin-converting enzyme 2 (ACE2) receptor, a homodimeric integral membrane protein expressed in the epithelial cells of lungs, heart, kidneys, and intestines[6]. Each ACE2 protomer consists of an N-terminal peptidase domain (PD), which interacts with the RBD of the S protein through an extended surface (Fig. 1a, c)[6, 7, 8]. Upon ACE2 binding, proteolytic cleavage of the S protein by the serine protease TMPRSS2 separates the S1 and S2 subunits[9]. The S2 protein exposes fusion peptides that insert into the host membrane and promote fusion with the viral membrane[4].

To prevent SARS-CoV-2 infection, there is a global effort to design neutralizing antibodies[10], nanobodies[11], peptide inhibitors[12], and small molecules[13] that target the ACE2 binding surface of the S protein. Yet, only a limited number of studies were performed to investigate critical interactions that facilitate S-ACE2 binding using MD simulations. Initial studies have constructed a homology model of SARS-CoV-2 RBD in complex with ACE2, based on the SARS-CoV crystal structure[8, 14] and performed conventional MD (cMD) simulations totaling 10 ns[15, 16] and 100 ns[17, 18] in length to estimate binding free energies[15, 16] and interaction scores[18]. More recent studies used the crystal structure of SARS-CoV-2 RBD in complex with ACE2 to perform coarse-grained[19] and all-atom[20, 21, 22, 23] MD simulations. The effect of the mutations

that disrupt close contact residues between SARS-CoV-2 RBD and ACE2 on binding free energy was investigated by post-processing of the MD trajectories[15, 16, 21, 22] or by using bioinformatic methods[20]. The work required to unbind the S protein from ACE2 would provide a more accurate estimate of the binding strength, but this has not been performed under low pulling velocities using the structure of SARS-CoV-2 RBD in complex with ACE2. In addition, systematic analysis of critical residues that stabilize S-ACE2 binding and how mutagenesis of these interaction sites reduces the binding strength and alters the way the S protein detaches from ACE2 under force have not yet been performed.

In this study, we performed a comprehensive set of all-atom MD simulations totaling 16.5 μs in length using the recently-solved structure of the RBD of the SARS-CoV-2 S protein in complex with the PD of ACE2[7]. Simulations were performed in the absence and presence of external force to investigate the binding characteristics and estimate the binding strength. These simulations showed additional interactions between RBD and PD domains to those observed in the crystal structure[7]. An extensive set of alanine substitutions and charge reversal mutations of the RBD amino acids involved in ACE2 binding were performed to quantify how mutagenesis of these residues weaken binding in the presence and absence of force in simulations. We showed that the hydrophobic end of RBD primarily stabilizes S-ACE2 binding, and targeting this site could potentially serve as an effective strategy to prevent SARS-CoV-2 infection.

Results

Interaction sites between the S protein and ACE2. To model the dynamic interactions of the S-ACE2 binding interface, we used the co-structure of RBD of the SARS-CoV-2 S protein in complex with the PD of human ACE2[7] (Fig. 1c). The structure was solvated in a water box that contains physiologically-relevant salt (150 mM NaCl) concentration. Two sets of cMD simulations, each of 100 ns in length, were performed to determine the formation of a salt bridge[24] and a hydrogen bond, as well as electrostatic and hydrophobic interactions between RBD and PD (Supplementary Table 1). A cutoff distance of 6 Å between the basic nitrogens and acidic oxygens was used to score a salt bridge formation[24]. For hydrogen bond formation, a maximum 3.5 Å distance between hydrogen bond donor and acceptor and a 30° angle between the hydrogen atom, the donor heavy atom, and the acceptor heavy atom was used[25]. Interaction pairs that satisfy the distance, but not the angle criteria were analyzed as electrostatic interactions. For hydrophobic interactions, a cutoff distance of 8 Å between the side chain carbon atoms was used[26, 27, 28]. Using these criteria, we identified eleven hydrophobic interactions (Fig. 2a), eight hydrogen bonds (Fig. 2b), two salt bridges and six electrostatic interactions (Fig. 2c) between RBD and PD. Observation frequencies were classified as high

and moderate for interactions that occur in 49% and above and between 15-48% of the total trajectory, respectively. F486 and Y489 of RBD formed hydrophobic interactions with F28, L79, M82, and Y83 of PD, while L455, F456, Y473, and A475 of RBD formed hydrophobic interactions with T27 of PD at high frequencies (Fig. 2d). Salt bridges between K417-D30 (RBD-PD) and E484-K31, and hydrogen bonds between N487-Y83, T500-D355, and Q493-E35 were observed at high frequencies, whereas hydrogen bonds Y449-D38, Q498-K353, T500-Y41, Y505-E37, and Q493-E35 were observed at moderate frequencies (Fig. 2d). Residue pairs Y453-H34, N487-Q24, T500-Y41, N501-K353, Q493-K31, and Y449-Q42 exhibited electrostatic interactions throughout the simulations (Fig. 2d).

The interaction network we identified in our cMD simulations were mostly consistent with reported interactions in the RBD-PD crystal structure[7]. However, our simulations identified four hydrogen bonds (Q498-K353, T500-D355, Y505-E37, and Q498-Q42), one hydrophobic interaction (L455-T27), and two electrostatic interactions (Y453-H34 and N501-K353) that are not present in the crystal structure. In turn, we did not detect frequent hydrogen bonding between G446-Q42, G502-K353, and Y505-R393 and an electrostatic interaction between G496-K353 observed in the crystal structure[7]. This discrepancy may be due to radically different thermodynamic conditions between crystallization solutions and cMD simulations[29].

We divided the RBD-PD interaction surface into three contact regions (CR1-3, Fig 2A-C)[23]. The contact region 2 (CR2) comprised significantly fewer interactions than the ends of the RBD binding surface (CR1 and CR3). Remarkably, 10 out of 13 interactions we detected in CR1 were hydrophobic, which were proposed to play a central role in anchoring of RBD to PD[23]. Unlike CR1, CR2 formed only a single hydrophobic interaction with PD, whereas CR3 did not form any hydrophobic interactions.

Unbinding of the S protein from ACE2 under force. To estimate the binding strength of the S protein to ACE2, we performed steered MD (SMD) simulations to pull RBD away from PD at a constant velocity of $2\ \text{Å}\ ns^{-1}$ along the vector pointing away from the binding interface (Fig. 3a). Steering forces were applied to the C_α atoms of the RBD residues on the binding interface, whereas C_α atoms of PD residues at the binding interface were kept fixed. These simulations were also repeated in the absence of ACE2 to account for the work done against viscous drag of water (Supplementary Fig. 1). The calculated average work against viscous drag was subtracted from all SMD work values reported in this study. Because part of the work applied is lost to the irreversible processes as we pull RBD away from PD at a finite velocity, the second law of thermodynamics indicates that unbinding free energy difference between the initial and final states cannot be larger than the average work required for unbinding. Therefore,

our calculations report relative changes in the binding free energy of wild-type (WT) and mutant RBD under the same velocity and thermodynamic conditions. In 20 SMD simulations (each 15 ns, totaling 300 ns in length, Supplementary Table 1), the average work applied to unbind SARS-CoV-2 RBD from PD was 64.0 ± 6.0 kcal/mol (mean ± s.d.), demonstrating that the S protein binds stably to ACE2 (Fig. 3b).

Mutagenesis of the S-ACE2 binding interface. To investigate the contribution of each of the 16 interactions we identified to the overall binding strength, we introduced point mutations on the RBD. Salt bridges were eliminated by charge reversals (K417E and E484K). We also replaced each interaction amino acid (except A475) with alanine (Supplementary Table 1) to disrupt the pairwise interactions[30], with minimal perturbations the protein backbone[31]. Two sets of cMD simulations (a total of 3.4 μs in length) were performed for each point mutant. We first quantified the root mean square fluctuation (RMSF) of the C_α atom of the RBD residues located on the PD binding surface (Fig. 3c). The rigid body motions were eliminated by aligning the RBD interaction surface of PD for each conformer (see Methods). 13 out of 17 mutations increased the residue fluctuations compared to WT (Supplementary Fig. 2a), suggesting that disrupting the interactions between RBD and PD results in floppier binding. Largest fluctuations were observed for 2 mutations in CR1 (F486A, and N487A), 2 mutations in CR3 (Y449A and Y505A) and 1 mutation in CR2 (L455A) (Fig. 3c). Mutation of these residues also increased the fluctuations in their neighboring region. While mutations in CR1 increased fluctuations in CR3 significantly, mutations in CR3 had little to no effect on the fluctuations in CR1 (Fig. 3d and Supplementary Fig. 2b).

We next performed SMD simulations modeling the unbinding of RBD of each point mutant from PD (20 simulations for each mutant, a total of 5.1 μs in length, Supplementary Table 1). F486A, Y489A, N487A, Y473A, E484K and Y505A mutations decreased the work requirement to unbind RBD-PD by 9-15% (Fig. 3e, f and Supplementary Fig. 3). We note that most of these mutations also led to the largest increase in residue fluctuations on the binding surface (Fig. 3c). 5 of these residues (F486, Y489, N487, Y473, and E484) are located in CR1, whereas Y505 is located in CR3. These results highlight the primary role of hydrophobic interactions in CR1 to stabilize the S-ACE2 binding.

To further characterize critical interactions of the S-ACE2 binding interface, we introduced double mutants to neighboring residues of RBD that form critical interactions with PD. We performed a total of 2.8 μs of cMD and 4.2 μs of SMD simulations for 14 double mutants (Supplementary Table 1). In particular, double mutants in CR1 resulted in 4 out of the 6 highest increase in RMSF (Fig. 4a and Supplementary Fig. 2). The F486A/N487A mutation at CR1

resulted in the largest increase in fluctuations in both CR1 and CR3 (Fig. 4a and Supplementary Fig. 2). In SMD simulations, 12 out of 14 double mutations also further decreased the average work to unbind RBD from PD (Fig. 4c, d and Supplementary Fig. 4). Similar to the RMSF analysis, double mutants in CR1 (F486A/N487A, E484A/Y489A, E484A/F486A, and L455A/F456A) resulted in 4 out of the 6 largest decreases in average work (Fig. 4d). A charge reversal of K417E in combination with either Q493A or Y453A also resulted in a large decrease in work values (Fig. 4d). We also used Jarzynski equality[32, 33] to construct the free energy profiles as a function of a reaction coordinate, referred to as the potential of mean force (PMF)[34]. Based on the estimated PMF (Supplementary Fig. 5), double mutants in CR1 resulted in the largest decrease in the binding energy by 31-21% compared to WT. Collectively, these results show that two salt bridges (E484-K31 and K417-D30) and the network of hydrophobic interactions in CR1 involving F486, Y489, Y473 and F456 residues are the most significant contributors of binding strength between the S protein and ACE2.

The hydrophobic end of RBD serves as the main anchor site for ACE2 binding. To test whether CR1 anchors RBD to PD[23], we investigated the order of events that result in detachment of RBD from PD in SMD simulations. The unbinding process appears to perform a zipper-like detachment starting from CR3 and ending at CR1 in 85% of the simulations (Fig. 5a). In only 15% of the simulations, CR3 released last from PD (Fig. 5a). Because unbinding simulations can reveal features characteristic for the reverse process of binding[35, 36, 37, 38, 39], these results suggest that CR1 binding is the first and critical event for the S protein binding to ACE2. Mutagenesis of the critical residues in CR1, in general, resulted in a substantial decrease in the percentages of unbinding events that terminate with the release of CR1 from PD. In alanine replacement of the hydrophobic residues (F486A, F487, and Y489), CR1 was released last for 60%, 55%, and 65% of the SMD simulations, respectively (Fig. 5b). The probability of CR1 to release last under force was further reduced in double mutants of E484A/F486A (50%) and L455A/F456A (55%) (Fig. 5b). Unlike these mutants, F456A and E484K mutants in CR1 increased the probability of CR1 to release last, but this could be attributed to a large increase in fluctuations in CR3 upon these mutations (Supplementary Fig. 2b). These results indicate that single and double mutants of the critical residues in CR1 substantially reduce the binding free energy of this region to ACE2.

S proteins of SARS-CoV-2 and SARS-CoV have similar binding strength to ACE2. It remains unclear whether higher infectivity of SARS-CoV-2 than SARS-CoV can be attributed to stronger interactions between S and ACE2 in SARS-CoV-2[2, 15]. To test this possibility, we performed two sets of MD simulations for the RBD of SARS-CoV S protein bound to the PD

of ACE2 (PDB ID: 2AJF[8]), and compared these results to that of SARS-CoV-2. Similar to SARS-CoV-2, RBD of SARS-CoV makes an extensive network of interactions with PD. We identified eleven hydrophobic interactions (Fig. 6a), six hydrogen bonds (Fig. 6b), and seven electrostatic interactions (Fig. 6c). Out of these 15 interactions, only 6 are conserved in SARS-CoV and the following mutations have taken place: L443/F456 (SARS-CoV/SARS-CoV-2), F460/Y473, P462/A475, P470/E484, L472/F486 V404/K417, N479/Q493, Y484/Q498, and T487/N501. Similar to SARS-CoV-2, L472 and Y475 of SARS-CoV RBD formed a total of seven hydrophobic interactions at a high frequency with the hydrophobic pocket of ACE2 (Fig. 6d). Unlike SARS-CoV-2, SARS-CoV RBD did not form any salt bridges with ACE2.

We next modeled the unbinding of RBD of SARS-CoV from PD by performing 20 SMD simulations (totaling 300 ns in length, Supplementary Table 1). The average total unbinding work of SARS-CoV (64.5 ± 12.2 kcal/mol, mean ± s.d., Fig. 6e) was identical but more broadly distributed than that of SARS-CoV-2 (64.0 ± 6.0 kcal/mol, Fig. 3b). Unlike SARS-CoV-2, CR1 released last from PD in only 40% of the unbinding events of RBD of SARS-CoV, whereas the unbinding of CR3 was the last event in the remaining 60% (Fig. 6f). These results indicate that the S protein binds stably to ACE2 in both SARS-CoV and SARS-CoV-2 and the higher infectivity of SARS-CoV-2 cannot be explained by an increase in binding strength. Higher variability in unbinding work values and the absence of a clear order in unbinding events of RBD of SARS-CoV suggest that SARS-CoV has a more variable binding mechanism to ACE2 than SARS-CoV-2.

Discussion

We performed an extensive set of *in silico* analysis to identify critical residues that facilitate binding of the RBD of the SARS-CoV-2 S protein to the human ACE2 receptor. Mutagenesis of these residues and pulling the RBD away from PD at a low velocity enabled us to estimate the free energy of binding and the order of events that result in the unbinding of RBD from PD. Our simulations showed that the PD interacting surface of RBD can be divided into three contact regions (CR1-3). Hydrophobic residues of CR1 strongly interact with the hydrophobic pocket of PD in both SARS-CoV and SARS-CoV-2. CR1 of SARS-CoV-2 also forms a salt bridge with ACE2 that is not present in SARS-CoV. Based on our SMD simulations, we did not observe a major difference in binding strength of the S protein to ACE2 between SARS-CoV and SARS-CoV-2, indicating that higher infectivity of SARS-CoV-2 is not due to tighter binding of S to the ACE2 receptor. These results are consistent with a recent MD simulation that applied the generalized Born and surface area continuum solvation approach (MM-GBSA)[22], coarse-grained simulations[19], and biolayer interferometry[2].

Our analysis suggests that CR1 is the main anchor site of the SARS-CoV-2 S protein to ACE2, and blocking the CR1 residues F456, Y473, E484, F486, N487, and Y489 could significantly reduce the binding affinity. Consistent with this prediction, llama based nanobodies H11-H4 and H11-D4 neutralize SARS-CoV-2[11] by each interacting with 50% of the critical residues we identified in each of CR1 and CR2. Furthermore, alpaca based nanobody Ty1 was shown to neutralize SARS-CoV-2[40] and among its primary interactions are E484 in CR1, and Q493 and Y449 in CR3, which were also determined as critical residues in our study. Similarly, the human neutralizing antibodies CV30[41], B38[41], CB6[41], and VH3-53[42, 43] are interacting with 50-100% of the critical residues identified in our study.

Experimental studies revealed that antibodies against SARS-CoV induce limited neutralizing activity against SARS-CoV-2[10, 23]. This may be attributed to the low sequence conservation of the CR1 region between SARS-CoV and SARS-CoV-2. In particular, the S protein of SARS-CoV-2 contains critical phenylalanine (F486) and glutamate (E484) residues not present in SARS-CoV, that form hydrophobic interactions and a salt bridge with ACE2, respectively. It remains to be determined whether this difference plays a role in higher infectivity of SARS-CoV-2 than SARS-CoV.

Our simulations show that single and double mutants of CR1 are not sufficient to disrupt the binding of RBD to ACE2, but reduce the binding free energy of this region. Because RBD makes multiple contacts with ACE2 through an extended surface, small molecules or peptides that target a specific region in the RBD-ACE2 interaction surface may not be sufficient to prevent binding of the S protein to ACE2. Instead, blocking of a larger surface of the CR1 region with a neutralizing antibody or nanobody is more likely to introduce steric constraints to prevent the S-ACE2 interactions.

Methods

MD simulations system preparation. For cMD simulations, the crystal structure of SARS-CoV-2 S protein RBD bound with ACE2 at 2.45 Å resolution (PDB ID: 6M0J)[7] was used as a template. The chloride ion, zinc ion, glycans, and water molecules in the crystal structure were kept in their original positions. Single and double point mutants were generated using the Mutator Plugin in VMD[44]. Each system was solvated in a water box (using the TIP3P water model) having 35 Å cushion in the positive x-direction and 15 Å cushions in other directions. This puts a 50 Å water cushion between the RBD-PD complex and its periodic image in the x-direction, creating enough space for unbinding simulations. Ions were added to neutralize the system and salt concentration was set to 150 mM to construct a physiologically relevant

environment. The size of each solvated system was ~164,000 atoms. All system preparation steps were performed in VMD[44].

Conventional MD simulations. All MD simulations were performed in NAMD 2.13[45] using the CHARMM36[46] force field with a time step of 2 fs. MD simulations were performed under N, P, T conditions. The temperature was kept at 310 K using Langevin dynamics with a damping coefficient of 1 ps^{-1}. The pressure was maintained at 1 atm using the Langevin Nosé-Hoover method with an oscillation period of 100 fs and a damping time scale of 50 fs. Periodic boundary conditions were applied. 12 Å cutoff distance was used for van der Waals interactions. Long-range electrostatic interactions were calculated using the particle-mesh Ewald method. For each system; first, 10,000 steps of minimization followed by 2 ns of equilibration was performed by keeping the protein fixed. The complete system was minimized for additional 10,000 steps, followed by 4 ns of equilibration by applying constraints on C_α atoms. Subsequently, these constraints were released and the system was equilibrated for an additional 4 ns before initiating the production runs. The length of the equilibrium steps is expected to account for the structural differences due to the radically different thermodynamic conditions of crystallization solutions and MD simulations[29]. MD simulations were performed in Comet and Stampede2 using ~8 million core-hours in total.

RMSF calculations. RMSF values were calculated as $\langle \Delta R_i^2 \rangle^{1/2} = \langle (R_i - \langle R_i \rangle)^2 \rangle^{1/2}$, where, $\langle R_i \rangle$ is the mean atomic coordinate of the ith C_α atom and R_i is its instantaneous coordinate.

SMD simulations. SMD[47] simulations were used to explore the unbinding process of RBD from ACE2 on time scales accessible to standard simulation lengths. SMD simulations have been applied to explore a wide range of processes, including domain motion[5, 48], molecule unbinding[49], and protein unfolding[50]. In SMD simulations, a dummy atom is attached to the center of mass of 'steered' atoms via a virtual spring and pulled at constant velocity along the 'pulling direction', resulting in force F to be applied to the SMD atoms along the pulling vector[45],

$$\mathbf{F} = -\nabla U \tag{1}$$

$$U = \frac{1}{2} k[\mathbf{v}t - (\mathbf{R} - \mathbf{R}_0) \cdot \mathbf{n}]^2 \tag{2}$$

where U is the guiding potential, k is the spring constant, $\mathbf{v}$ is the pulling velocity, t is time, $\mathbf{R}$ and $\mathbf{R}_0$ are the coordinates of the center of mass of steered atoms at time t and 0, respectively, and $\mathbf{n}$ is the direction of pulling[45]. Total work (W) performed for each simulation was evaluated by integrating F over displacement ξ along the pulling direction as $W = \int_0^{\xi} F(\xi) d\xi$.

In SMD simulations of SARS-CoV-2, C_α atoms of ACE2 residues S19-S43, T78-P84, Q325-N330, G352-I358, and P389-R393 were kept fixed, whereas C_α atoms of RBD residues K417-I418, G446-F456, Y473-A475, and N487-Y505 were steered (Fig. 3a). Steered atoms were selected as the region comprising the interacting residues. For SARS-CoV SMD simulations the same ACE2 residues were kept fixed. However, two slightly different steered atoms selections were applied: i) Using the same residue positions as for SARS-CoV-2, which are V404-I405, T433-L443, F460-S461, and N473-Y491, and ii) selecting the region comprising the interacting residues, which areT433-L443, F460-D463, and N473-Y491. The total number of fixed and steered atoms were identical in all simulations. The pulling direction was selected as the vector pointing from the center of mass of fixed atoms to the center of mass of steered atoms. The pulling direction also serves as the reaction coordinate ξ for free energy calculations. Each SMD simulation was performed for 15 ns using a $2\ \text{Å}\ ns^{-1}$ pulling velocity. At a spring constant of $100\ kcal\ mol^{-1}\ \text{Å}^{-2}$, the center of mass of the steered atoms followed the dummy atom closely while the spring was still soft enough to allow small deviations. For each system, 20 conformations were sampled with a 10 ns frequency from their cMD simulations (10 conformers from each set of the cMD simulations listed in Supplementary Table 1 MD1-33 a-b). These conformations served as 20 separate starting conformations, $\mathbf{R}_0$, for each set of SMD simulations (Supplementary Table 1 MD1-33 c-d).

Potential of mean force for unbinding of RBD. Work values to unbind RBD from ACE2 at low pulling velocities along the reaction coordinate were analyzed using Jarzynski equality, which provides a relation between equilibrium free energy differences and the work performed through non-equilibrium processes[32, 33, 34]:

$$e^{-\Delta F/k_B T} = \langle e^{-W/k_B T} \rangle \qquad (3)$$

where ΔF is the Helmholtz free energy, k_B is the Boltzmann constant and T is the temperature. Because work values sampled in our SMD simulations differ more than1 $k_B T$ (Supplementary Figs. 3,4), the average work calculated in equation (3) will be dominated by small work values that are only rarely sampled. For a finite (N) number of SMD simulations, the term $-k_B T \ln\left(\sum_{i=1}^{N} e^{-W_i/k_B T}/N\right)$ did not converge to $\langle e^{-W/k_B T} \rangle$. Thus, equation (3) provides an upper bound on ΔF, which was used as an estimate of the PMF.

Data availability

Data and the analysis software are available from the corresponding author upon request.

References

1. Ren L-L, *et al.* Identification of a novel coronavirus causing severe pneumonia in human: a descriptive study. *Chinese medical journal*, (2020).

2. Walls AC, Park Y-J, Tortorici MA, Wall A, McGuire AT, Veesler D. Structure, Function, and Antigenicity of the SARS-CoV-2 Spike Glycoprotein. *Cell*, (2020).

3. Belouzard S, Millet JK, Licitra BN, Whittaker GR. Mechanisms of coronavirus cell entry mediated by the viral spike protein. *Viruses* **4**, 1011-1033 (2012).

4. Kirchdoerfer RN, *et al.* Stabilized coronavirus spikes are resistant to conformational changes induced by receptor recognition or proteolysis. *Scientific reports* **8**, 1-11 (2018).

5. Gur M, Taka E, Yilmaz SZ, Kilinc C, Aktas U, Golcuk M. Conformational transition of SARS-CoV-2 spike glycoprotein between its closed and open states. *The Journal of Chemical Physics* **153**, 075101 (2020).

6. Yan R, Zhang Y, Li Y, Xia L, Guo Y, Zhou Q. Structural basis for the recognition of the SARS-CoV-2 by full-length human ACE2. *Science*, (2020).

7. Lan J, *et al.* Structure of the SARS-CoV-2 spike receptor-binding domain bound to the ACE2 receptor. *Nature*, 1-9 (2020).

8. Li F, Li W, Farzan M, Harrison SC. Structure of SARS coronavirus spike receptor-binding domain complexed with receptor. *Science* **309**, 1864-1868 (2005).

9. Hoffmann M, *et al.* SARS-CoV-2 cell entry depends on ACE2 and TMPRSS2 and is blocked by a clinically proven protease inhibitor. *Cell*, (2020).

10. Yi C, *et al.* Key residues of the receptor binding motif in the spike protein of SARS-CoV-2 that interact with ACE2 and neutralizing antibodies. *Cellular & Molecular Immunology*, 1-10 (2020).

11. Huo J, *et al.* Neutralizing nanobodies bind SARS-CoV-2 spike RBD and block interaction with ACE2. *Nature Structural & Molecular Biology*, (2020).

12. Han Y, Král P. Computational Design of ACE2-Based Peptide Inhibitors of SARS-CoV-2. *ACS nano*, (2020).

13. de Oliveira OV, Rocha GB, Paluch AS, Costa LT. Repurposing approved drugs as inhibitors of SARS-CoV-2 S-protein from molecular modeling and virtual screening. *Journal of Biomolecular Structure and Dynamics*, 1-14 (2020).

14. Song W, Gui M, Wang X, Xiang Y. Cryo-EM structure of the SARS coronavirus spike glycoprotein in complex with its host cell receptor ACE2. *PLoS pathogens* **14**, e1007236 (2018).

15. He J, Tao H, Yan Y, Huang S-Y, Xiao Y. Molecular Mechanism of Evolution and Human Infection with SARS-CoV-2. *Viruses* **12**, 428 (2020).

16. Armijos-Jaramillo V, Yeager J, Muslin C, Perez-Castillo Y. SARS-CoV-2, an evolutionary perspective of interaction with human ACE2 reveals undiscovered amino acids necessary for complex stability. *Evolutionary Applications*, (2020).

17. Zou J, *et al.* Computational Prediction of Mutational Effects on the SARS-CoV-2 Binding by Relative Free Energy Calculations. (2020).

18. Brielle ES, Schneidman-Duhovny D, Linial M. The SARS-CoV-2 exerts a distinctive strategy for interacting with the ACE2 human receptor. *Viruses* **12**, 497 (2020).

19. Bai C, Warshel A. Critical Differences Between the Binding Features of the Spike Proteins of SARS-CoV-2 and SARS-CoV. *The Journal of Physical Chemistry B* **124**, 5907-5912 (2020).

20. Dehury B, Raina V, Misra N, Suar M. Effect of mutation on structure, function and dynamics of receptor binding domain of human SARS-CoV-2 with host cell receptor ACE2: a molecular dynamics simulations study. *Journal of Biomolecular Structure and Dynamics*, 1-15 (2020).

21. Ali A, Vijayan R. Dynamics of the ACE2–SARS-CoV-2/SARS-CoV spike protein interface reveal unique mechanisms. *Scientific Reports* **10**, 1-12 (2020).

22. Li Y, *et al.* The MERS-CoV receptor DPP4 as a candidate binding target of the SARS-CoV-2 spike. *Iscience*, 101160 (2020).

23. Wang Y, Liu M, Gao J. Enhanced receptor binding of SARS-CoV-2 through networks of hydrogen-bonding and hydrophobic interactions. *Proceedings of the National Academy of Sciences*, (2020).

24. Beckstein O, Denning EJ, Perilla JR, Woolf TB. Zipping and unzipping of adenylate kinase: atomistic insights into the ensemble of open↔ closed transitions. *Journal of molecular biology* **394**, 160-176 (2009).

25. Durrant JD, McCammon JA. HBonanza: a computer algorithm for molecular-dynamics-trajectory hydrogen-bond analysis. *Journal of Molecular Graphics and Modelling* **31**, 5-9 (2011).

26. Stock P, Utzig T, Valtiner M. Direct and quantitative AFM measurements of the concentration and temperature dependence of the hydrophobic force law at nanoscopic contacts. *Journal of colloid and interface science* **446**, 244-251 (2015).

27. Manavalan P, Ponnuswamy P. A study of the preferred environment of amino acid residues in globular proteins. *Archives of biochemistry and biophysics* **184**, 476-487 (1977).

28. Stavrakoudis A, Tsoulos IG, Shenkarev ZO, Ovchinnikova TV. Molecular Dynamics Simulation of Antimicrobial Peptide Arenicin-2: b-Hairpin Stabilization by Noncovalent Interactions.

29. Pullara F, Wenzhi M, GÜR M. Why protein conformers in molecular dynamics simulations differ from their crystal structures: a thermodynamic insight. *Turkish Journal of Chemistry* **43**, 394-403 (2019).

30. Weiss GA, Watanabe CK, Zhong A, Goddard A, Sidhu SS. Rapid mapping of protein functional epitopes by combinatorial alanine scanning. *Proceedings of the National Academy of Sciences* **97**, 8950-8954 (2000).

31. Bradshaw RT, Patel BH, Tate EW, Leatherbarrow RJ, Gould IR. Comparing experimental and computational alanine scanning techniques for probing a prototypical protein–protein interaction. *Protein Engineering, Design & Selection* **24**, 197-207 (2011).

32. Jarzynski C. Equilibrium free-energy differences from nonequilibrium measurements: A master-equation approach. *Physical Review E* **56**, 5018 (1997).

33. Jarzynski C. Nonequilibrium equality for free energy differences. *Physical Review Letters* **78**, 2690 (1997).

34. Park S, Khalili-Araghi F, Tajkhorshid E, Schulten K. Free energy calculation from steered molecular dynamics simulations using Jarzynski's equality. *The Journal of chemical physics* **119**, 3559-3566 (2003).

35. Le L, Lee EH, Hardy DJ, Truong TN, Schulten K. Molecular dynamics simulations suggest that electrostatic funnel directs binding of Tamiflu to influenza N1 neuraminidases. *PLoS Comput Biol* **6**, e1000939 (2010).

36. Izrailev S, Stepaniants S, Balsera M, Oono Y, Schulten K. Molecular dynamics study of unbinding of the avidin-biotin complex. *Biophysical journal* **72**, 1568-1581 (1997).

37. Yang L-J, Zou J, Xie H-Z, Li L-L, Wei Y-Q, Yang S-Y. Steered molecular dynamics simulations reveal the likelier dissociation pathway of imatinib from its targeting kinases c-Kit and Abl. *PLoS One* **4**, e8470 (2009).

38. Liu X, Xu Y, Wang X, Barrantes FJ, Jiang H. Unbinding of nicotine from the acetylcholine binding protein: steered molecular dynamics simulations. *The Journal of Physical Chemistry B* **112**, 4087-4093 (2008).

39. Shen J, Li W, Liu G, Tang Y, Jiang H. Computational insights into the mechanism of ligand unbinding and selectivity of estrogen receptors. *The Journal of Physical Chemistry B* **113**, 10436-10444 (2009).

40. Hanke L, *et al.* An alpaca nanobody neutralizes SARS-CoV-2 by blocking receptor interaction. *Nature Communications* **11**, 4420 (2020).

41. Hurlburt NK, *et al.* Structural basis for potent neutralization of SARS-CoV-2 and role of antibody affinity maturation. *Nature communications* **11**, 1-7 (2020).

42. Barnes CO, *et al.* SARS-CoV-2 neutralizing antibody structures inform therapeutic strategies. *Nature*, (2020).

43. Wu NC, *et al.* An alternative binding mode of IGHV3-53 antibodies to the SARS-CoV-2 receptor binding domain. *Cell reports* **33**, 108274 (2020).

44. Humphrey W, Dalke A, Schulten K. VMD: visual molecular dynamics. *Journal of molecular graphics* **14**, 33-38 (1996).

45. Phillips JC, *et al.* Scalable molecular dynamics with NAMD. *Journal of computational chemistry* **26**, 1781-1802 (2005).

46. Best RB, *et al.* Optimization of the additive CHARMM all-atom protein force field targeting improved sampling of the backbone ϕ, ψ and side-chain $\chi1$ and $\chi2$ dihedral angles. *Journal of chemical theory and computation* **8**, 3257-3273 (2012).

47. Isralewitz B, Gao M, Schulten K. Steered molecular dynamics and mechanical functions of proteins. *Current opinion in structural biology* **11**, 224-230 (2001).

48. Izrailev S, Crofts AR, Berry EA, Schulten K. Steered molecular dynamics simulation of the Rieske subunit motion in the cytochrome bc1 complex. *Biophysical journal* **77**, 1753-1768 (1999).

49. Eskici G, Gur M. Computational design of new peptide inhibitors for amyloid beta (Aβ) aggregation in Alzheimer's disease: application of a novel methodology. *Plos one* **8**, (2013).

50. Lu H, Isralewitz B, Krammer A, Vogel V, Schulten K. Unfolding of titin immunoglobulin domains by steered molecular dynamics simulation. *Biophysical journal* **75**, 662-671 (1998).

51. Casalino L, *et al.* Beyond Shielding: The Roles of Glycans in the SARS-CoV-2 Spike Protein. *ACS Central Science* **6**, 1722-1734 (2020).

Acknowledgments

We gratefully acknowledge the support of the COVID-19 HPC Consortium (Grant number: TG-MCB200070), and Extreme Science and Engineering Discovery Environment (XSEDE).

Author contributions

Mert Gur (M.G.) and A.Y. initiated the project. M.G. supervised the project. E.T., S.Z.Y., Mert Golcuk (M.Go), C.K., U.A., and M.G. performed molecular dynamics simulations. E.T., S.Z.Y., M.Go, C.K., U.A., A.Y., and M.G. prepared the manuscript.

Competing interests

The authors declare no competing interests.

Figures

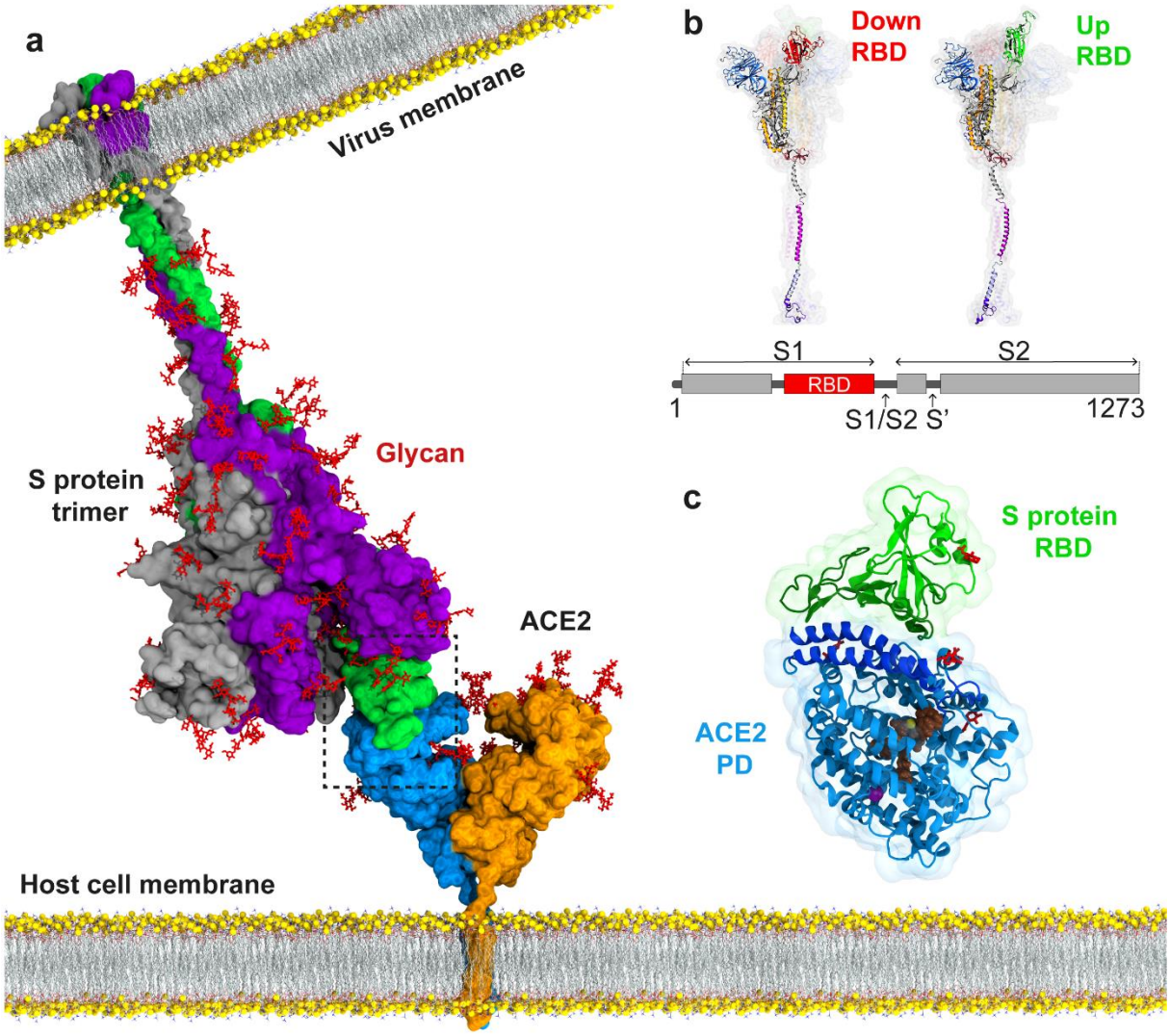

Fig. 1. Atomic model for binding of the SARS-CoV-2 S protein to the ACE2 receptor on the host cell membrane. a The structure of the full-length S protein in complex with ACE2. The S protein is a homotrimer (green, purple, and grey) and embedded into the viral membrane. ACE2 is a homodimer (blue and orange) and embedded into the host cell membrane. The full length structure of the S protein in complex with ACE2 was modeled using the full length S protein model [51] and the crystal structure of the S protein RBD in complex with ACE2 (PDB ID: 6M17). Both proteins were manually inserted into the membrane by their transmembrane domains. **b** The structure of an S protomer in the down and up position of its RBD. S1/S2 and S2' are the cleavage sites of the S protomer upon ACE2 binding. **(C)** MD simulations were performed for RBD of the S protein in complex with the PD of ACE2. Catalytic residues of ACE2, glycans, and Zn^{+2} and Cl^{-} ions are shown in brown, red, yellow and purple, respectively.

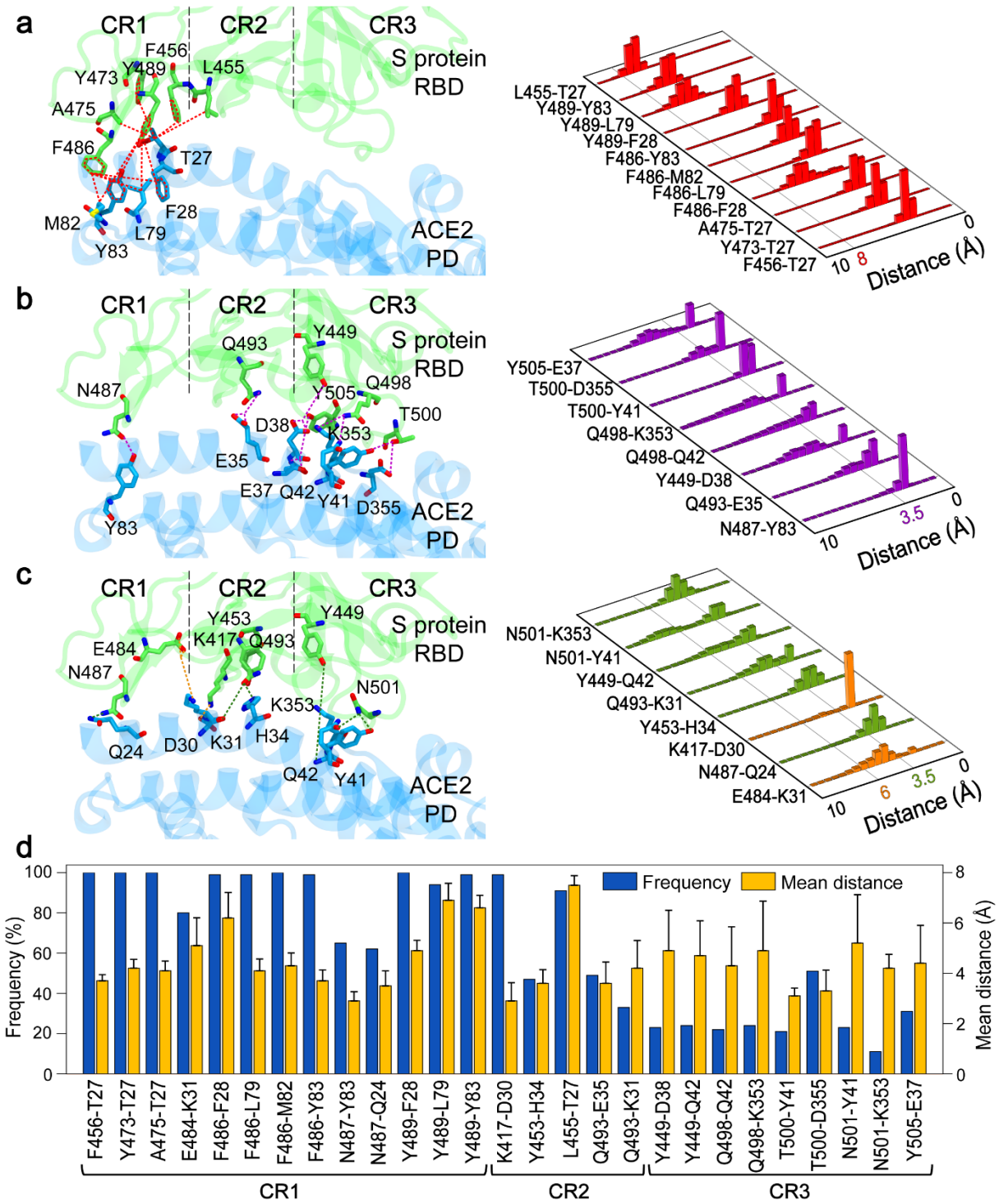

Fig. 2. Interactions between RBD of the SARS-CoV-2 S protein and PD of ACE2. a Hydrophobic interactions **b** Hydrogen bonds, and **c** Salt bridges and electrostatic interactions, between RBD (green) and PD (blue) are shown on a conformation obtained from MD simulations in the left panels. The interaction surface is divided into three distinct regions (CR1-3). Normalized distributions of the distances between the amino-acid pairs that form hydrophobic interactions (red), hydrogen bonds (purple), salt bridges (orange), and electrostatic interactions (green) are shown in the right panels. Lines with colored numbers represent

maximum cutoff distances for these interactions. **d** The frequencies and mean distances of the pairwise interactions of the RBD-PD binding interface. Error bars represent s.d.

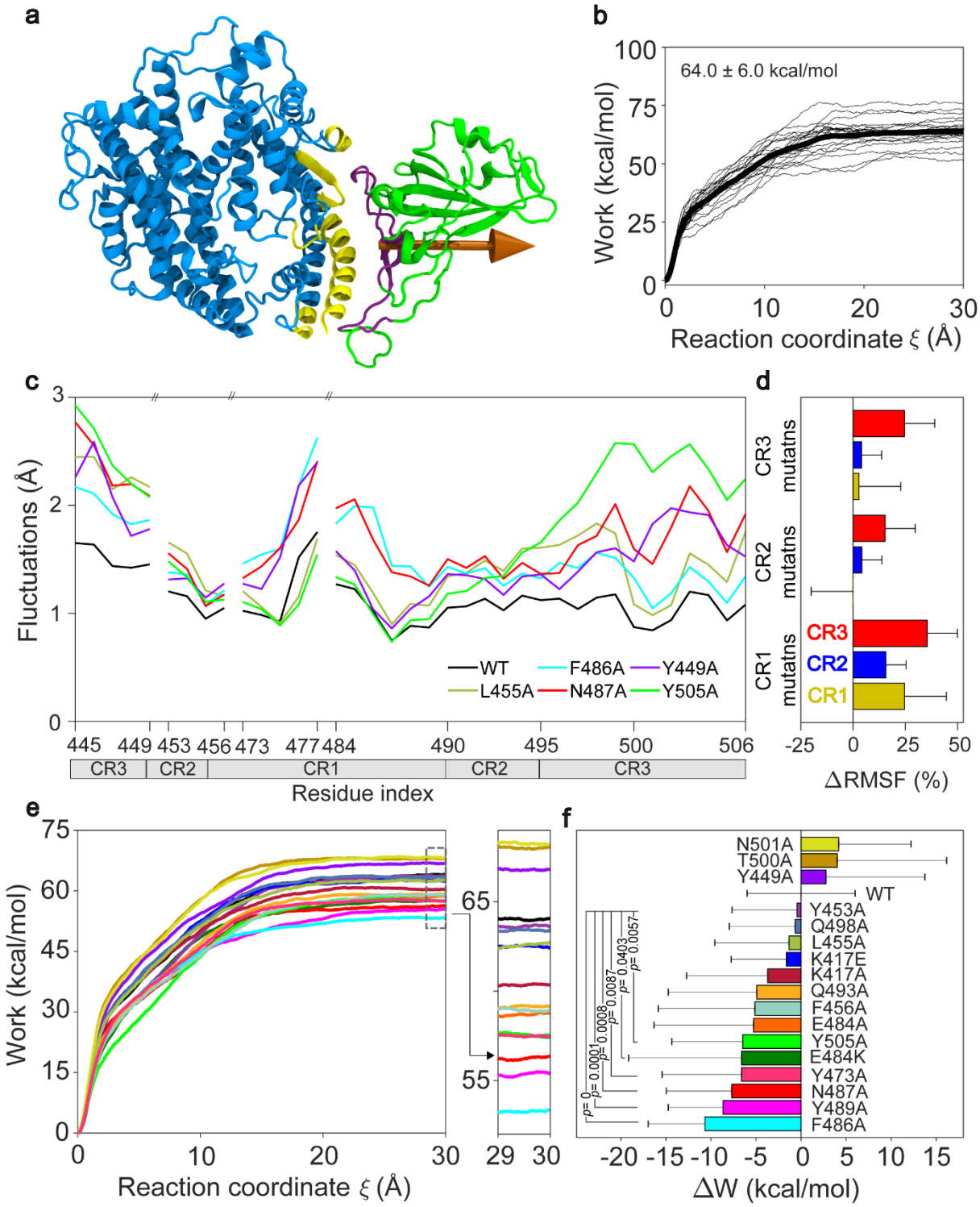

Fig. 3. Point mutations in the ACE2 binding surface of RBD reduce the binding strength. **a** In SMD simulations, C_α atoms of PD residues (yellow) were fixed, whereas C_α atoms of RBD (purple) were steered. The orange arrow on the RBD (green) shows the SMD pulling vector,

which was taken as the reaction coordinate. **b** Distribution of work applied during unbinding of RBD from PD. The thick line represents the average work values. **c** RMSF of RBD residues located on the PD binding surface of WT and point mutants. **d** Point mutants in CR1, CR2 and CR3 alter the RMSF values of the C_α atoms of CR1, CR2 and CR3 regions relative to WT. **e** Over 20 SMD simulations, the average work required to move RBDs along the reaction coordinate are shown for the WT and point mutants. Work profiles in the region ξ = 29 – 30 Å are shown on the right panel. **f** The change in the average unbinding work of point mutants compared to WT. *P* values were calculated using a two-tailed Student's t-test. *P* values larger than 0.05 are not shown. Error bars represent s.d.

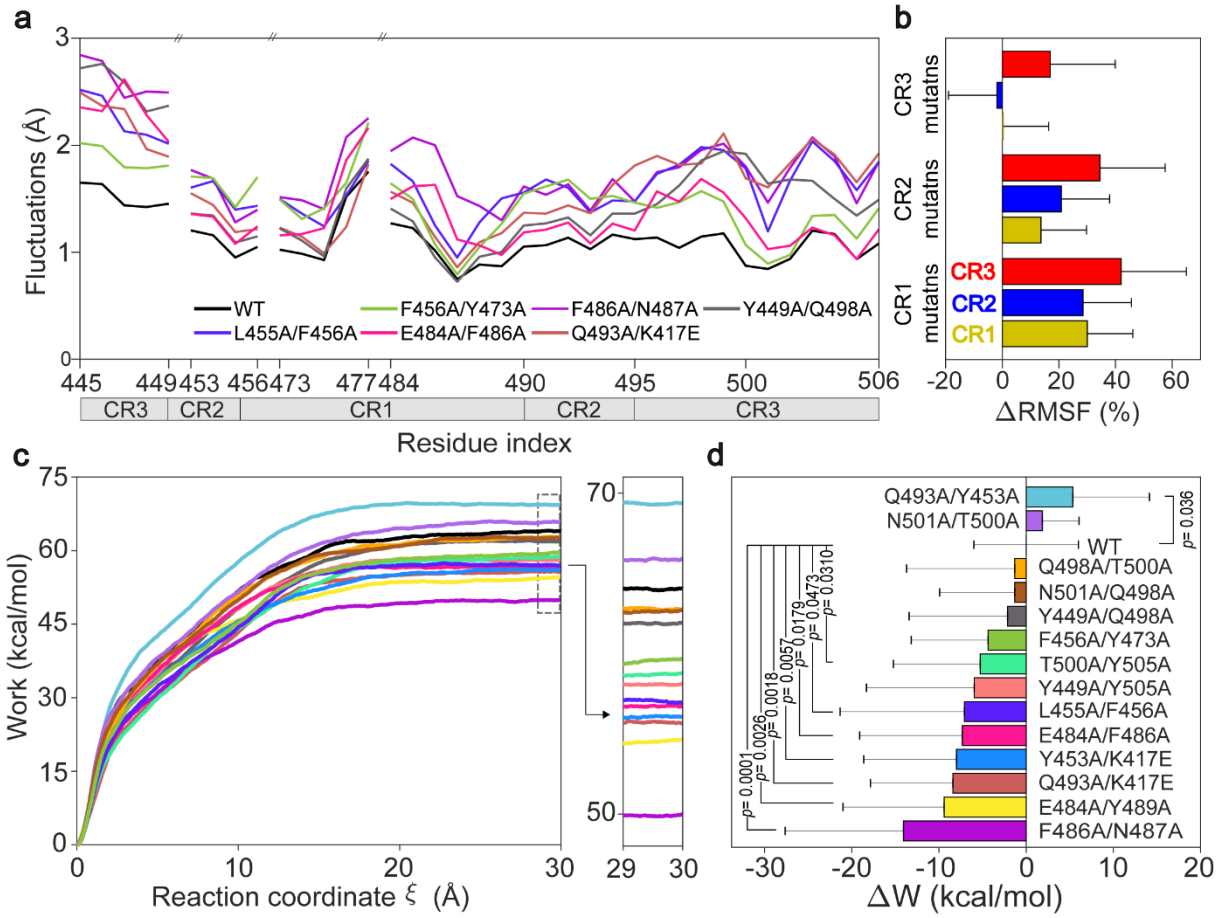

Fig. 4. Double mutants of the PD binding surface of RBD more strongly decrease its binding strength. a Residue fluctuations at the ACE2 binding surface for WT and double mutants of the SARS-CoV-2 S protein. **b** Double mutants in CR1, CR2 and CR3 alter the RMSF values of the Cα atoms of CR1, CR2 and CR3 regions relative to WT. **c** Over 20 SMD simulations, the average work required to move RBD along the reaction coordinate is shown for the WT and double mutants. Work profiles in the region ξ = 29 – 30 Å are shown on the right panel. **d** The change in the average unbinding work of double mutants compared to WT. *P* values were calculated using a two-tailed Student's t-test. Error bars represent s.d.

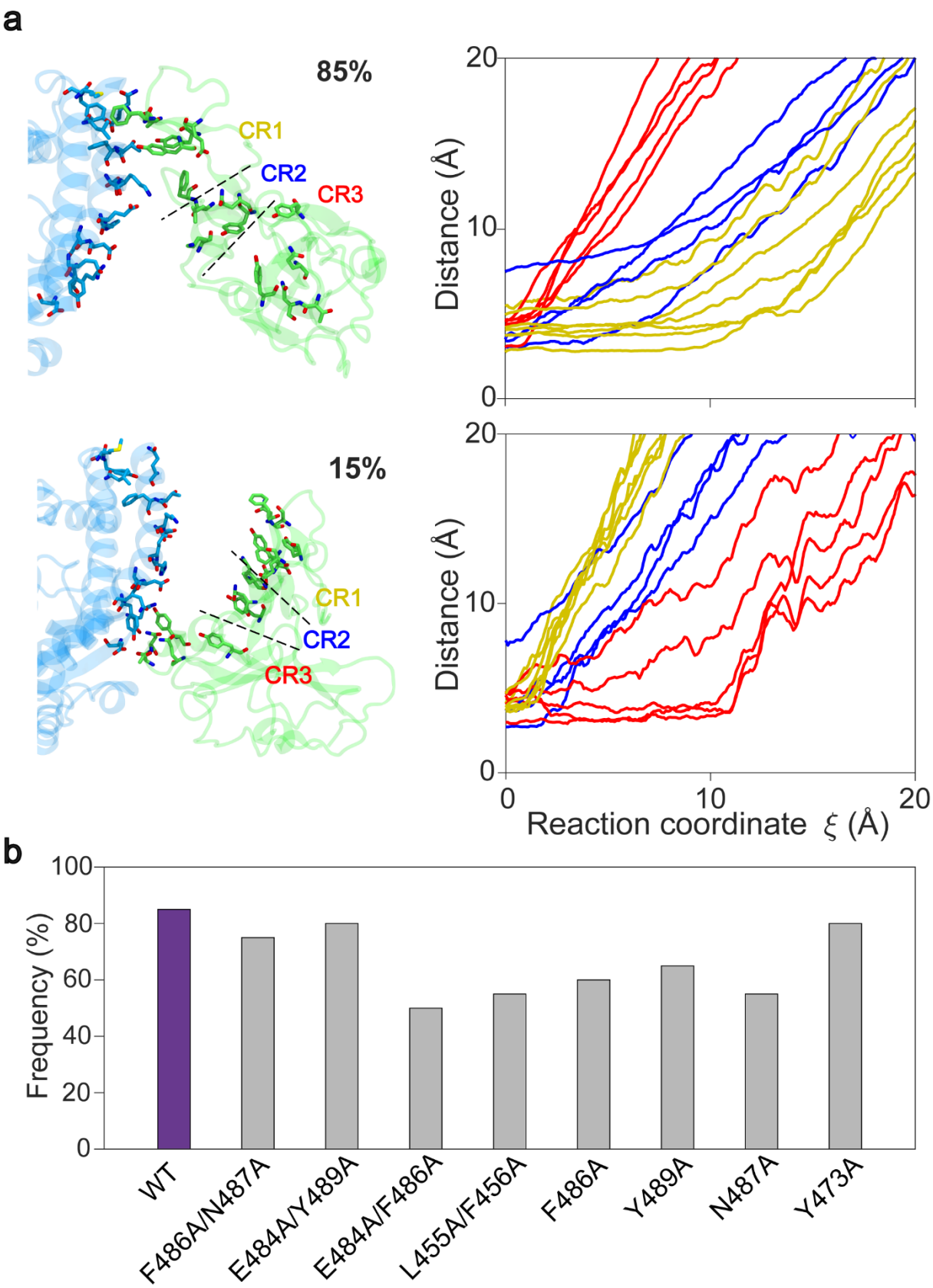

Fig. 5. CR1 releases last from PD under force. a (Top left) Representative conformer shows CR1 releases last when RBD was pulled away from PD at a constant velocity of 2 Å/ns. (Top right) Displacement of the critical residues in CR1 (yellow), CR2 (blue), and CR3 (red) along

the reaction coordinate, averaged over 17 SMD simulations. (Bottom left) Representative conformer shows CR3 releases last when RBD was pulled away from PD in SMD simulations. (Bottom right) Displacement of the critical residues in CR1 (yellow), CR2 (blue), and CR3 (red) along the reaction coordinate, averaged over 3 SMD simulations. **b** The percentage of SMD trajectories of WT and mutant RBD, in which CR1 released last from PD when pulled at a constant velocity.

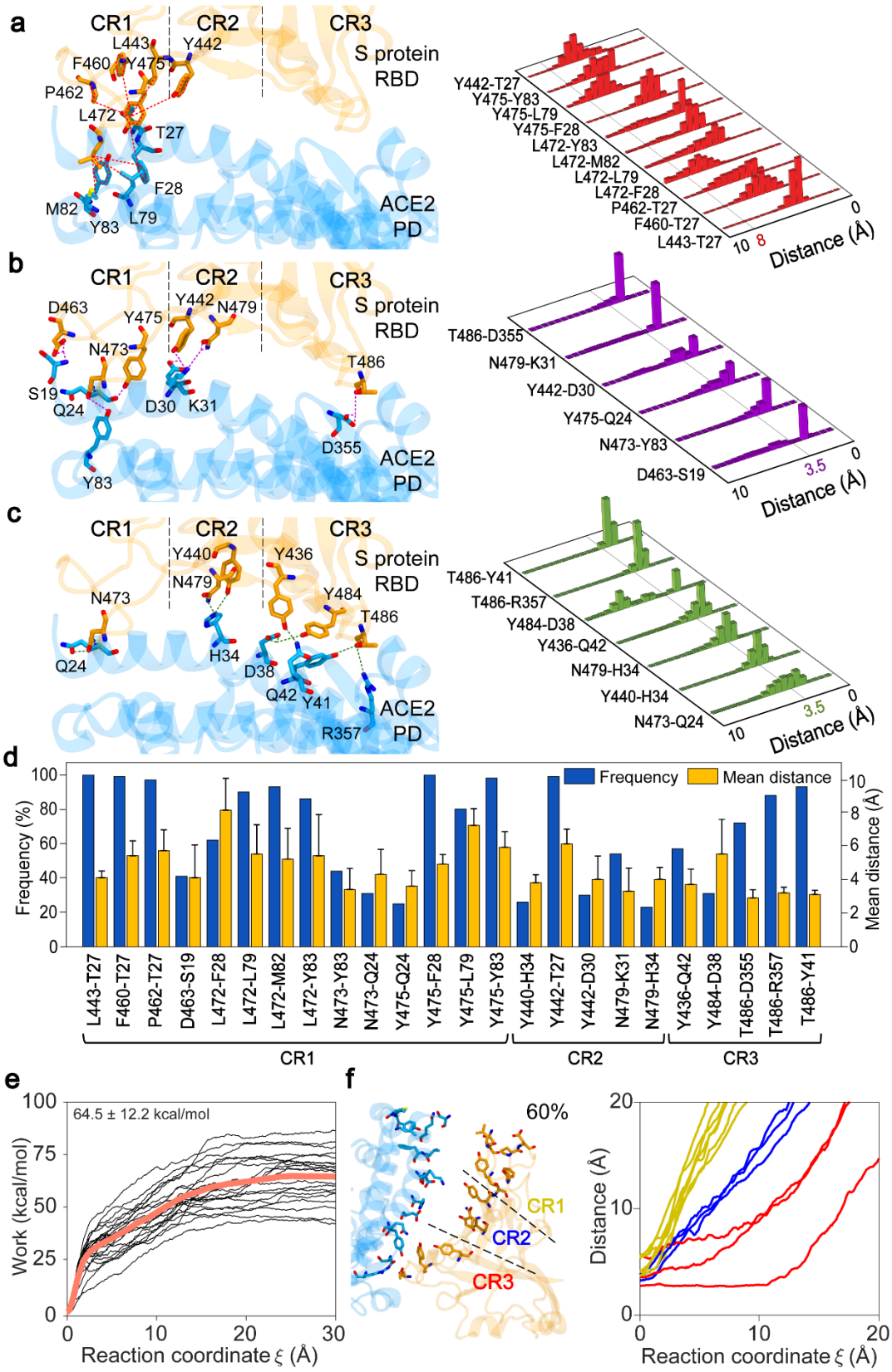

Fig. 6. Interactions between RBD of the SARS-CoV S protein and PD of ACE2. a Hydrophobic interactions **b** Hydrogen bonds, and **c** Electrostatic interactions, between RBD (orange) and PD (blue) are shown on a conformation obtained from MD simulations in the left panels. Normalized distributions of the distances between the amino-acid pairs that form

hydrophobic interactions (red), hydrogen bonds (purple), and electrostatic interactions (green) are shown in the right panels. Lines with colored numbers represent maximum cutoff distances for these interactions. **d** The frequencies and mean distances of the pairwise interactions of the SARS-CoV S protein and ACE2 binding interface. **e** Distribution of work applied during unbinding of RBD from PD. The thick line represents the average work values. **f** (Left) Representative conformer shows CR3 releases last when RBD was pulled away from PD at a constant velocity of 2 Å/ns. (Right) Displacement of the critical residues in CR1 (yellow), CR2 (blue), and CR3 (red) along the reaction coordinate, averaged over 12 SMD simulations. Error bars represent s.d.

Supplementary Materials

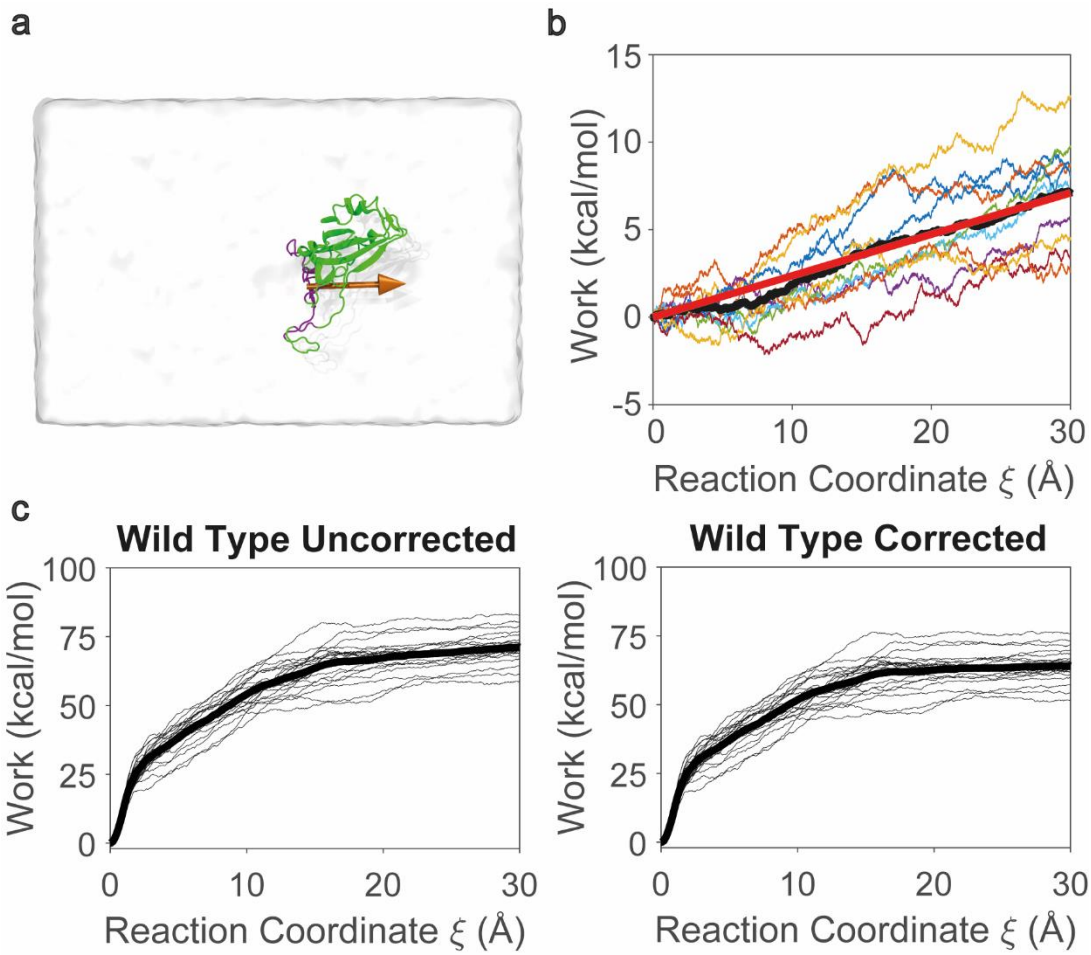

Fig. S1. Work done against viscous drag of water in SMD simulation. a In SMD simulations, Cα atoms of RBD (purple) were steered. The orange arrow on the RBD (green) shows the SMD pulling vector, which was taken as the reaction coordinate. **b** Work values obtained from pulling RBD in the absence of ACE2. Black line is the average work from 10 different SMD simulations. Red line represents the work done against the viscous drag of SMD simulation and was defined as the line passing through the initial and last data point of the black curve. **c** Distribution of work values are shown for uncorrected (work values as obtained from the SMD simulations) and corrected (work done against viscous drag of water is subtracted from SMD work values) are shown. Thick line represents the mean work values.

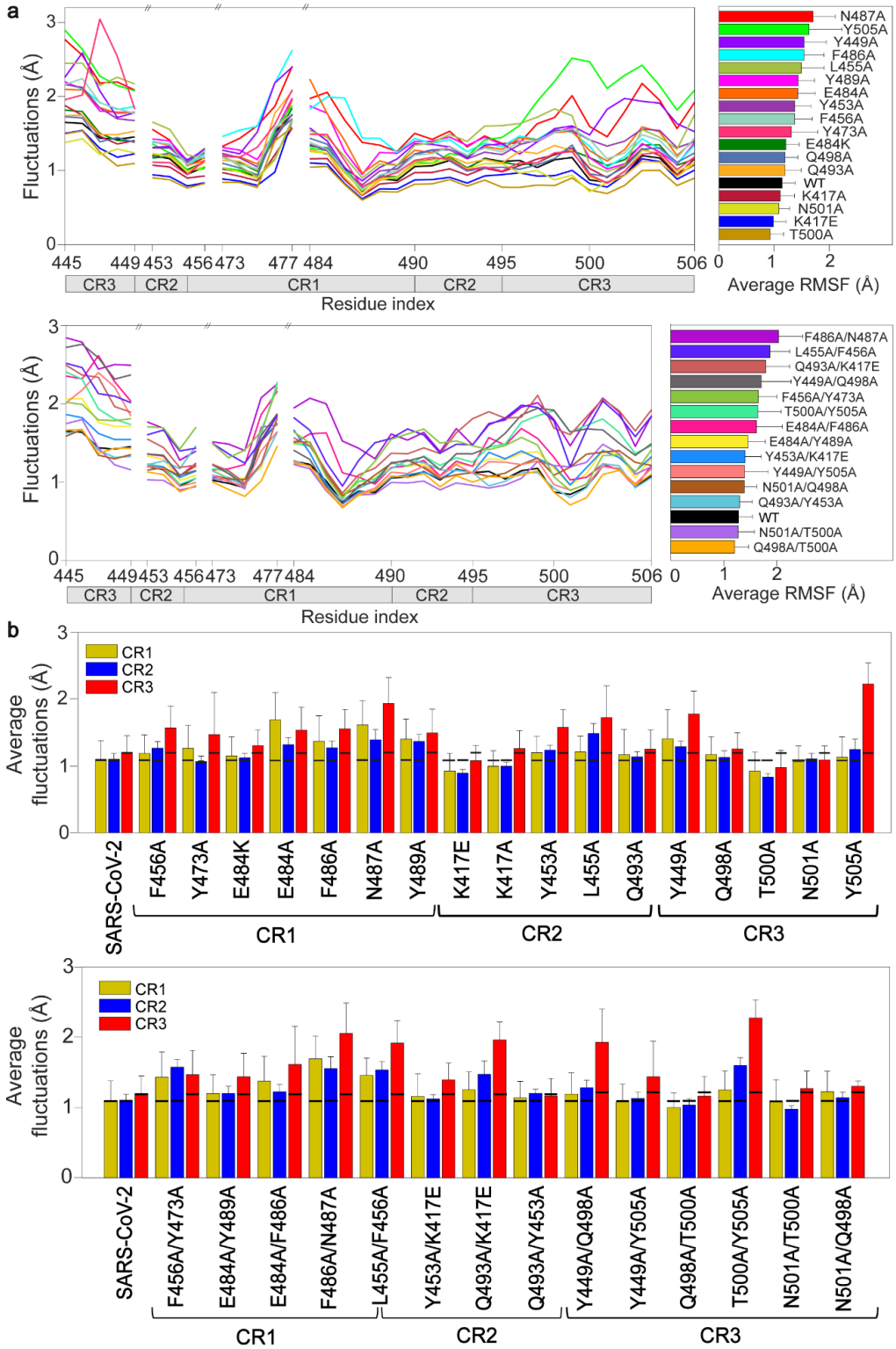

Fig. S2. RMSF values of single and double mutants of RBD of SARS-CoV-2. a RMSF of RBD residues located on the PD binding surface of WT and point mutants. **b** Average RMSF values of the Cα atoms at CR1, CR2, and CR3 for the WT and mutant SARS-CoV-2 RBD in complex with ACE2 PD. The black lines in each bar show the average RMSF values in CR1, CR2, and CR3 for the WT. Error bars represent s.d.

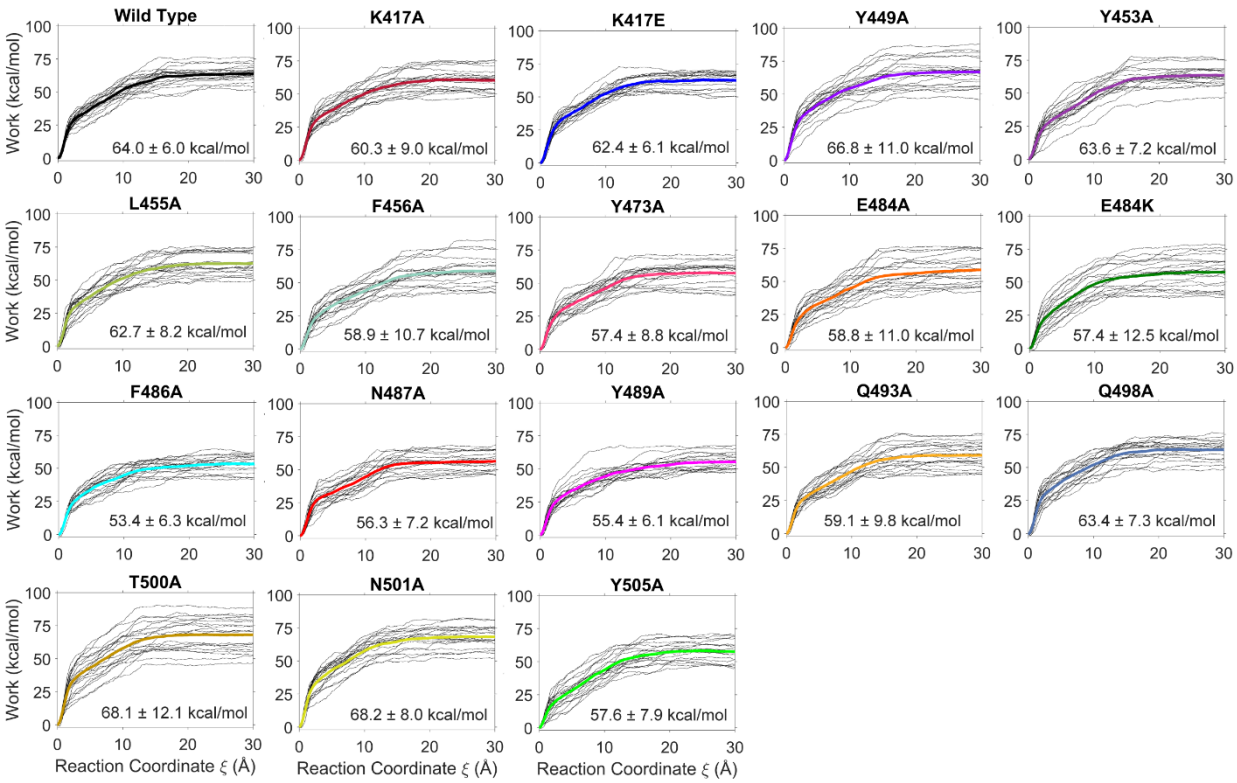

Fig. S3. Distribution of work values obtained from SMD simulations for each single point mutant system of RBD of SARS-CoV-2. Thick lines represent the average work values of each system.

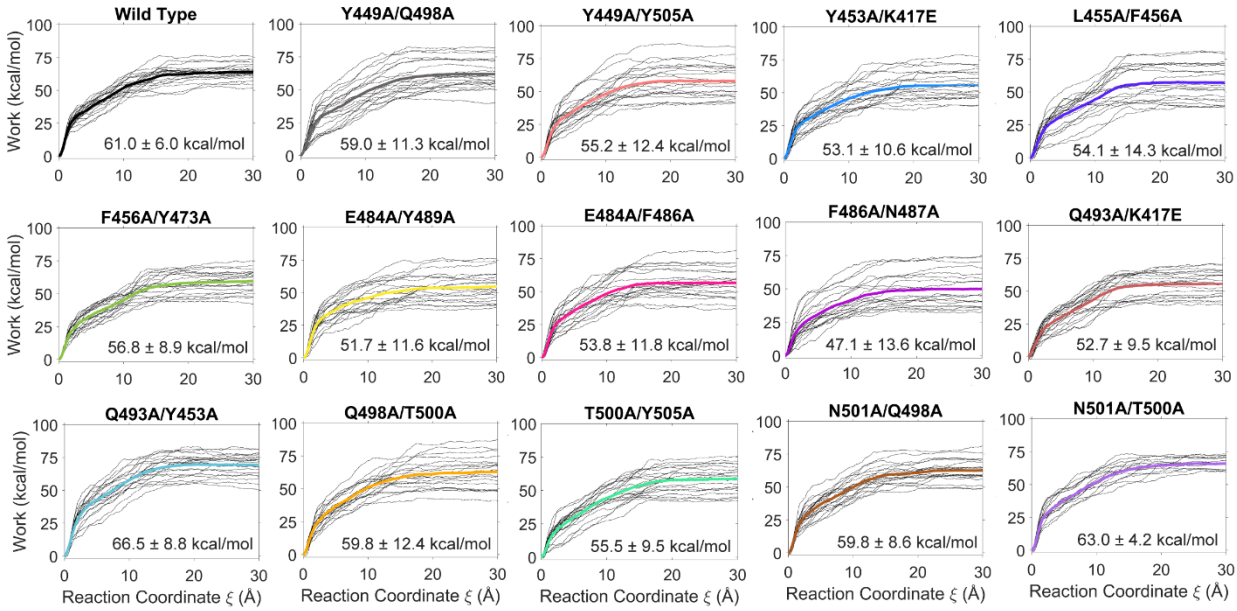

Fig. S4. Distribution of work values obtained from SMD simulations for each double point mutant system of RBD of SARS-CoV-2. Thick lines represent the average work values of each system.

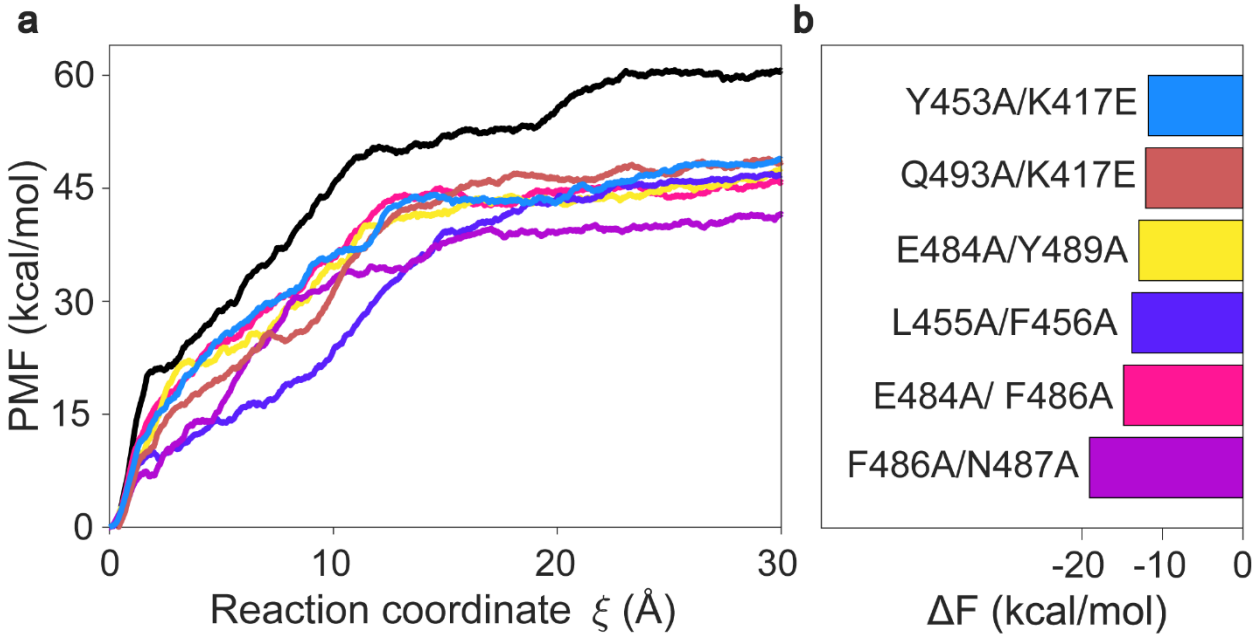

Fig. S5. PMF and ΔF values of WT and six point mutants of RBD of SARS-CoV-2. a PMF values of WT and 6 double mutants with lowest unbinding work values. **b** ΔF values of these mutants are calculated from Jarzynski equality.

Table S1. Starting conformations and durations of the MD simulations performed.

Run ID	Initial state	RBD sequence	Simulation Type	Simulation Duration (ns)
1a-b	RBD-ACE2 complex (6M0J)	WT SARS-CoV-2	MD	(a) 100, (b) 100
1c-d	Final conformers of MD 1a-b	WT SARS-CoV-2	SMD	(c) 150, (d) 150
2a-b	RBD-ACE2 complex (6M0J)	K417A	MD	(a) 100, (b) 100
2c-d	Final conformers of MD 2a-b	K417A	SMD	(c) 150, (d) 150
3a-b	RBD-ACE2 complex (6M0J)	K417E	MD	(a) 100, (b) 100
3c-d	Final conformers of MD 3a-b	K417E	SMD	(c) 150, (d) 150
4a-b	RBD-ACE2 complex (6M0J)	E484A	MD	(a) 100, (b) 100
4c-d	Final conformers of MD 4a-b	E484A	SMD	(c) 150, (d) 150
5a-b	RBD-ACE2 complex (6M0J)	E484K	MD	(a) 100, (b) 100
5c-d	Final conformers of MD 5a-b	E484K	SMD	(c) 150, (d) 150
6a-b	RBD-ACE2 complex (6M0J)	Y489A	MD	(a) 100, (b) 100
6c-d	Final conformers of MD 6a-b	Y489A	SMD	(c) 150, (d) 150
7a-b	RBD-ACE2 complex (6M0J)	N487A	MD	(a) 100, (b) 100
7c-d	Final conformers of MD 7a-b	N487A	SMD	(c) 150, (d) 150
8a-b	RBD-ACE2 complex (6M0J)	F486A	MD	(a) 100, (b) 100
8c-d	Final conformers of MD 8a-b	F486A	SMD	(c) 150, (d) 150
9a-b	RBD-ACE2 complex (6M0J)	Y505A	MD	(a) 100, (b) 100
9c-d	Final conformers of MD 9a-b	Y505A	SMD	(c) 150, (d) 150
10a-b	RBD-ACE2 complex (6M0J)	Q453A	MD	(a) 100, (b) 100
10c-d	Final conformers of MD 10a-b	Q453A	SMD	(c) 150, (d) 150
11a-b	RBD-ACE2 complex (6M0J)	T500A	MD	(a) 100, (b) 100
11c-d	Final conformers of MD 11a-b	T500A	SMD	(c) 150, (d) 150
12a-b	RBD-ACE2 complex (6M0J)	Y449A	MD	(a) 100, (b) 100
12c-d	Final conformers of MD 12a-b	Y449A	SMD	(c) 150, (d) 150
13a-b	RBD-ACE2 complex (6M0J)	Q493A	MD	(a) 100, (b) 100
13c-d	Final conformers of MD 13a-b	Q493A	SMD	(c) 150, (d) 150
14a-b	RBD-ACE2 complex (6M0J)	Q498A	MD	(a) 100, (b) 100
14c-d	Final conformers of MD 14a-b	Q498A	SMD	(c) 150, (d) 150
15a-b	RBD-ACE2 complex (6M0J)	N501A	MD	(a) 100, (b) 100
15c-d	Final conformers of MD 15a-b	N501A	SMD	(c) 150, (d) 150
16a-b	RBD-ACE2 complex (6M0J)	L455A	MD	(a) 100, (b) 100
16c-d	Final conformers of MD 16a-b	L455A	SMD	(c) 150, (d) 150
17a-b	RBD-ACE2 complex (6M0J)	F456A	MD	(a) 100, (b) 100
17c-d	Final conformers of MD 17a-b	F456A	SMD	(c) 150, (d) 150
18a-b	RBD-ACE2 complex (6M0J)	Y473A	MD	(a) 100, (b) 100
18c-d	Final conformers of MD 18a-b	Y473A	SMD	(c) 150, (d) 150
19a-b	RBD-ACE2 complex (6M0J)	F486A/N487A	MD	(a) 100, (b) 100
19c-d	Final conformers of MD 19a-b	F486A/N487A	SMD	(c) 150, (d) 150
20a-b	RBD-ACE2 complex (6M0J)	E484A/Y489A	MD	(a) 100, (b) 100
20c-d	Final conformers of MD 20a-b	E484A/Y489A	SMD	(c) 150, (d) 150
21a-b	RBD-ACE2 complex (6M0J)	E484A/F486A	MD	(a) 100, (b) 100

21c-d	Final conformers of MD 21a-b	E484A/F486A	SMD	(c) 150, (d) 150
22a-b	RBD-ACE2 complex (6M0J)	T500A/Y505A	MD	(a) 100, (b) 100
22c-d	Final conformers of MD 22a-b	T500A/Y505A	SMD	(c) 150, (d) 150
23a-b	RBD-ACE2 complex (6M0J)	Y453A/K417E	MD	(a) 100, (b) 100
23c-d	Final conformers of MD 23a-b	Y453A/K417E	SMD	(c) 150, (d) 150
24a-b	RBD-ACE2 complex (6M0J)	Q493A/Y453A	MD	(a) 100, (b) 100
24c-d	Final conformers of MD 24a-b	Q493A/Y453A	SMD	(c) 150, (d) 150
25a-b	RBD-ACE2 complex (6M0J)	Q493A/K417E	MD	(a) 100, (b) 100
25c-d	Final conformers of MD 25a-b	Q493A/K417E	SMD	(c) 150, (d) 150
26a-b	RBD-ACE2 complex (6M0J)	Y449A/Q498A	MD	(a) 100, (b) 100
26c-d	Final conformers of MD 26a-b	Y449A/Q498A	SMD	(c) 150, (d) 150
27a-b	RBD-ACE2 complex (6M0J)	Y449A/Y505A	MD	(a) 100, (b) 100
27c-d	Final conformers of MD 27a-b	Y449A/Y505A	SMD	(c) 150, (d) 150
28a-b	RBD-ACE2 complex (6M0J)	Q498A/T500A	MD	(a) 100, (b) 100
28c-d	Final conformers of MD 28a-b	Q498A/T500A	SMD	(c) 150, (d) 150
29a-b	RBD-ACE2 complex (6M0J)	N501A/T500A	MD	(a) 100, (b) 100
29c-d	Final conformers of MD 29a-b	N501A/T500A	SMD	(c) 150, (d) 150
30a-b	RBD-ACE2 complex (6M0J)	N501A/Q498A	MD	(a) 100, (b) 100
30c-d	Final conformers of MD 30a-b	N501A/Q498A	SMD	(c) 150, (d) 150
31a-b	RBD-ACE2 complex (6M0J)	L455A/F456A	MD	(a) 100, (b) 100
31c-d	Final conformers of MD 31a-b	L455A/F456A	SMD	(c) 150, (d) 150
32a-b	RBD-ACE2 complex (6M0J)	F456A/Y473A	MD	(a) 100, (b) 100
32c-d	Final conformers of MD 32a-b	F456A/Y473A	SMD	(c) 150, (d) 150
33a-b	RBD-ACE2 complex (6M0J)	WT SARS-CoV	MD	(a) 100, (b) 100
33c-d	Final conformers of MD 33a-b	WT SARS-CoV	SMD	(c) 150, (d) 150